Research article

"Synthesis and characterization of mesoporous V–Mo-MCM-41 nanocatalysts: Enhancing efficiency in oxalic acid synthesis"

Jasem Suliman Al Ebraheem [*], Mohammad Nour Ahmad Alkhoder [**], Reem Hani Tulaimat

Department of Chemistry, Faculty of Science, Albaath University, Homs, Syria

ABSTRACT

Mesoporous V–Mo-MCM-41 nano molecular sieves were synthesized via the direct hydrothermal method, employing tetraethyl orthosilicate (TEOS) as a silica source and cetyl-trimethylammonium bromide (CTAB) as a surfactant template. Comprehensive characterization through N_2-adsorption (BET), Fourier-transform infrared spectroscopy (FT-IR), X-ray diffraction (XRD), and scanning electron microscopy-energy-dispersive X-ray spectroscopy (SEM-EDX) confirmed the mesoporous nature of the catalysts, revealing variations in specific surface area and a significant pore diameter of 6.3 nm, enhancing their versatility for various chemical transformations. The nanoscale structure was further validated through XRD analysis and SEM images. The catalytic efficiency of V–Mo-MCM-41 was demonstrated by synthesizing oxalic acid from molasses, and a response surface methodology (RSM) study on four key variables revealed a maximum yield of 83 % within 1 h using minimal sulfuric acid, showcasing the effectiveness of the prepared catalysts.

1. Introduction

Catalysis is a necessary process that helps convert raw materials into high-value, sustainable, and economically viable chemical products. This makes it an essential tool for addressing global energy and environmental challenges [1]. Chemical manufacturing processes in advanced countries rely heavily on catalysts, which contribute over 80 % to these processes and about one-fourth to their overall Gross Domestic Product (GDP) [2]. Heterogeneous catalysis is the preferred method for about 90 % of catalytic chemical reactions [3,4], The development of new materials based on support modification has been driven by the need to improve the efficiency of industrial catalysts in various processes. The aim is to create a suitable porous structure.One of the most common heterogeneous catalysts is zeolite, which was prominent as an extensively studied microporous compound [5–7]. Despite their notable characteristics, such as high adsorption capacity and large specific surface area, zeolites face a significant limitation that hinders their practical applications. The restricted pore sizes, typically ranging from 0.5 to 1.2 nm, pose challenges in accommodating large molecules. Researchers have been focusing on developing new strategies and techniques for preparing and synthesizing novel porous materials that meet the needs of the chemical industry. This is necessary because the geometric factor of the pores in zeolites is not

---

always suitable for accelerating the flow and efficient reaction of compounds [8–11].

In order to create materials with large pores, it is necessary to use more prominent structure-directing agents (templates) during the manufacturing process. Several porous materials, such as $AlPO_4^{-8}$ and VPI^{-5}, were synthesized in the 1980s with pore diameters ranging from 0.8 to 1.3 nm. The pores were irregularly spaced and widely distributed in size [12], and these materials had low thermal and hydrothermal stability [13]. The material UTD^{-1} was synthesized by the researcher Balkus and colleagues and exhibited high silica content and stability. However, there were challenges in removing the structure-directing agent, limiting its practical applications [14]. Large-pore crystalline materials are not readily applicable in catalytic processes despite significant progress. Today, the most promising materials in the porous domain appear to be those discovered in the late 1980s and early 1990s [13]. In the year 1988, the researcher Yangisawa and colleagues synthesized a new mesoporous material by introducing stearyl trimethylammonium chloride ions as structure-directing agents in layered silicates known as kanemite ($NaHSi_2O_5.3H_2O$), The obtained mesoporous material exhibited a pore diameter ranging between 2 and 4 nm [15].

In 1992, researchers at Mobil Oil Company developed a new mesoporous material called Mobil Composition of Matter (MCM). The objective behind synthesizing these materials was to increase the pore diameter of zeolites. Since then, several molecular mesoporous sieves have been prepared, following the liquid crystal templating (LCT) mechanism [16,17]. These materials are surfactant-based directing agents made up of polar and nonpolar components. The importance of templates lies in their ability to control the pore diameter by altering the hydrocarbon chain length in the template material, these molecular mesoporous sieves are prepared by condensing and polymerizing a silicate source around the formed micelles resulting from the dissolution of the surfactant material, which aggregates in cylindrical shapes. The template is then removed through a calcination process [10,18]. These materials differ significantly from zeolites because the pore walls are non-crystalline [13,19]. MCM-41, which signifies Mobil's 41st material composition, holds significant importance within the family of Molecular Mesoporous Sieves (MMS). It is highly valued for its well-defined hexagonal structure, ease of synthesis, customizable pore size, efficient adsorption of large organic molecules due to its spacious pores, narrow pore size distribution, high specific surface area (1500 m^2/g), uniform pore distribution ranging from 2 to 10 nm, as well as its remarkable chemical and thermal stability [18–25]. The impressive properties of MCM-41 have established it as a significant and versatile material in catalytic applications. Its exceptionally high specific surface area has led to its utilization as an effective adsorbent for water purification [26], mainly removing organic pollutants, such as eliminating phenol and chlorophenol contaminants [27–29]. Furthermore, MCM-41 has demonstrated its utility in drug delivery systems, showcasing its potential for controlled and targeted drug release [30–32]. In recent years, intensive efforts have been made to enhance the catalytic efficiency of MCM-41 due to its limited catalytic applications resulting from a low number of active sites [33], moderate framework structure [34], and low hydrothermal stability in aqueous solutions [27]. The methodology adopted to improve the effectiveness of MCM-41 involves two methods:

The first involves the incorporation of active transition metal ions into the MCM-41 structure through direct hydrothermal synthesis of a mixture containing the silicate source, template, and the desired metal salt. Alternatively, it may involve subsequent treatment of the pre-synthesized mesoporous material. Consequently, the newly integrated silica catalysts in metals have enhanced catalytic properties and the capability to oxidize large organic molecules. The integration of metal particles on the internal surface of the medium-sized particles creates active sites for both acidic and oxidative-reductive functionalities. These active sites can be utilized in various chemical reactions across multiple categories [3,35–38].

For instance, the acidity of MCM-41 has been enhanced by incorporating zirconium metal [39]. Among the transition metals widely incorporated into mesoporous silica of the MCM-41 type, vanadium and molybdenum have been notably integrated due to their superior catalytic properties. Supported vanadium oxide species and mesoporous materials containing vanadium are recognized as highly active and selective catalysts for catalytic transformations, such as selective oxidation of hydrocarbons and hydrogenation [40,41]. Vanadium was introduced into the MCM-41 framework for the first time by Reddy et al. through a direct hydrothermal synthesis approach, using vanadyl sulfate as the vanadium precursor. The catalytic performance of the V-MCM-41 catalyst was evaluated in oxidation reactions of cyclooctane and 1-naphthol, using hydrogen peroxide as the oxidant. The results demonstrated the catalyst's effectiveness in producing new chemical compounds [42]. Supported molybdenum oxide catalysts exhibited high efficiency in the oxidation of ethanol, methanol, propylene, and butane, as well as in sulfur removal from petroleum feedstocks [43].

The Ni–Mo/MCM-41 catalyst was employed in sulfur removal from thiophene and chlorine removal from polychlorinated biphenyls [44]. The selectivity of vanadium oxides can be significantly enhanced by combining them with MoO_3. V_2O_5–MoO_3 catalysts were used in catalytic oxidation of benzene to maleic anhydride [45]. Mixed vanadium and molybdenum oxides appeared as highly active and selective oxidative catalysts [46]. Researcher Selvaraj studied the catalytic performance of the V–Mo-MCM-41 catalyst prepared by the direct hydrothermal method in the oxidation process of o-xylene to phthalic anhydride, showing the highest activity when (Si/(V + Mo) = 46) [47]. Additionally, researcher Abbas Teimouri and colleagues prepared several samples of the catalyst (MoO_3/V_2O_5/MCM-41) by the impregnation method, and the prepared catalysts exhibited high efficiency in the oxidation of dibenzothiophene for sulfur removal using H_2O_2 as the oxidant compared to previously used catalysts [48]. It can be concluded that mixed catalysts containing vanadium and molybdenum are essential in catalysis chemistry. These catalysts can achieve superior catalytic activity and high selectivity in numerous crucial industrial catalytic transformations. Many studies have focused on correlating catalytic activity with the nanoparticle size in addition to the geometric structure of the resulting catalyst [49]. Catalytic activity increases with decreasing particle size, as it has been found that smaller nanoparticles are more active [50]. Therefore, the second method involves reducing the particle size to create nanoporous catalysts with nano dimensions. Nanocatalysts come in different shapes, such as nanoclusters, nanospheres, and nanosheets [51], and have properties that combine the benefits of both homogeneous and heterogeneous catalysis. As a result, nano-mesoporous silica is highly versatile and has received significant research attention, particularly in separation techniques, heterogeneous catalysis, water purification, and adsorption [52–54].

Oxalic acid is vital in various industries as an essential chemical compound. It finds wide-ranging applications, including bleaching, marble polishing, rust removal, and cleaning metal surfaces, thanks to its exceptional ability to dissolve iron oxides [55,56]. In recent years, oxalic acid has been used in processing phosphate rocks to extract phosphate, a crucial component in producing phosphate fertilizers essential for global food security [57,58]. Furthermore, studies have highlighted oxalic acid as one of the organic acids that effectively extract valuable metals such as V, Mo, and Ni from catalysts used in refining processes. The reaction between these metals and oxalic acid, which functions as an extraction agent, frees the metals from the catalysts and allows for their effective separation and high recovery rate [59]. Previous studies have reported the preparation of oxalic acid through various methods, Depending on the raw materials used. Still, the most important of them are the oxidation of carbohydrates by nitric acid [60], the Fermentation of carbohydrates into oxalic acid using Aspergillus niger [61], The decomposition of sodium formate, Which can be prepared using glycol, ethylene, molasses, sugars, propylene, plant residues, and wood tar as raw materials [62]. Pentavalent vanadium oxide has been identified as the most effective catalyst for carbohydrate oxidation, mainly glucose. Studies have indicated that the support material has a significant impact and can enhance the efficiency of pentavalent vanadium oxide [63,64]. Some researchers attempted to synthesize oxalic acid without a catalyst and reported highly unsatisfactory results. In contrast, Deshpande and his colleague, in 1979, successfully prepared oxalic acid from sugar as the starting material. They utilized V_2O_5/Fe^{3+} as a catalyst, nitric acid as an oxidant, and around 50 % sulfuric acid in the liquid phase. The reaction lasted 4 h, yielding approximately 71 % oxalic acid [64]. In 1989, Douglas-fir bark was used as a raw material for producing oxalic acid using nitric acid (62.5 vol%) with a reaction time of 8 h, yielding approximately 38 % oxalic acid [63]. In 2001, researcher Metin Guru and colleagues synthesized oxalic acid from molasses as a raw material using a catalyst (7.5 % V_2O_5 on porous silica gel). A yield of 78 % oxalic acid was obtained using 1.95g of sulfuric acid, 5g of nitric acid, and 0.7 mg of V_2O_5 per 1g of molasses, with a reaction time of 8 h [60].

In previous studies, large amounts of sulfuric acid were employed during the reaction, along with extended reaction times. Therefore, this nano-catalyst was developed as an effective tool for oxalic acid synthesis, aiming to reduce the quantity of sulfuric acid used, minimize reaction time, and improve overall yield.Given the versatility and efficiency of V_2O_5 and MoO_3 catalysts in various vital reactions, along with the exceptional properties exhibited by these supported catalysts on Si-MCM-41, it is anticipated that V–Mo-MCM-41 nano-catalysts will also demonstrate excellent catalytic activity in glucose oxidation reactions. However, to the best of our knowledge, no study has been conducted using bimetallic catalysts supported on MCM-41 supports for glucose oxidation reactions. Instead, a few works have been reported on using V_2O_5 catalysts to oxidize glucose to produce oxalic acid.

The scope of this study is divided into two parts: the first part aims to enhance the catalytic activity of the MCM-41 material by incorporating varying amounts of active centers V and Mo. This part of the study aims to develop improved nano-catalysts that enhance the material's performance as a catalytic unit. Appropriate characterization techniques will be employed to understand and analyze the physical and chemical properties of the designed nano-catalysts.

The second part will explore the catalytic activity in glucose oxidation reactions, which have not been studied before. Molasses contains a high percentage of glucose, estimated at around 31 %. Consequently, using molasses for oxalic acid production is crucial in the industry, providing an efficient and economical method to obtain this important compound for various industrial applications.

This will involve numerical and statistical analysis and simulation of oxalic acid production. Additionally, it will identify the factors influencing the yield of oxalic acid. The study aims to identify new and potential applications for these prepared materials by analyzing the various and interactive effects among the variables to balance performance and cost for the studied materials.

2. Experimental section

2.1. Materials

The V–Mo-MCM-41 catalysts were synthesized using different chemicals obtained from BDH Company. Tetraethyl orthosilicate (TEOS, 98 %) was used as the silica source, cetyltrimethylammonium bromide (CTAB, 99 %) served as a template, ammonium metavanadate (NH_4VO_3, 98 %) was used as the vanadium precursor, sodium molybdate ($Na_2MoO_4.2H_2O$, 99.5 %) acted as the molybdenum source, oxalic acid ($H_2C_2O_4.2H_2O$, 99.5 %), and sodium hydroxide (NaOH, 99 %). The catalyst's performance was evaluated using molasses, a secondary product obtained during sugar extraction from sugar beets containing (31%wt) of glucose. Commercial nitric acid (HNO_3, 49 %) and sulfuric acid (H_2SO_4, 98 %) were employed, along with the prepared catalysts.

2.2. Preparation of V–Mo-MCM-41 nanocatalyst

The V–Mo-MCM-41 catalysts were synthesized using the direct hydrothermal method under self-generated pressure inside the autoclave. The preparation involved using different ratios of (Si/V + Mo), following a modified approach based on the methodology outlined in references [65–67].

The preparation process for the catalyst with a ratio (Si/V + Mo = 34) involved several sequential steps. Firstly, 1g of cetyltrimethylammonium bromide (CTAB) was dissolved in 15 ml of distilled water at 30 °C to ensure the formation of a proper solution. Then, 2.4 ml of tetraethylorthosilicate (TEOS) was slowly and gradually added with vigorous stirring for 2 h, resulting in the formation of a homogeneous gel with a molar ratio (Sur/Si < 1). In the next step, 0.0368g of ammonium metavanadate and 0.0853g of oxalic acid (molar ratio 1:2) were dissolved in 6 ml of distilled water. The resulting yellow solution was heated to 100 °C, yielding a stable blue solution. This blue solution was added dropwise to the gel under vigorous stirring for 30 min. Subsequently, 0.0262g of sodium molybdate was dissolved in 5 ml of distilled water, and the resulting solution was added dropwise to the gel with stirring for 30 min. The pH value was adjusted to 11 by adding 1 N sodium hydroxide solution to the mixture, followed by stirring the suspension for 2 h to

eliminate any insoluble components. The resulting suspension was transferred to a 100 ml stainless steel autoclave lined with Teflon and heated to 130 °C for 48 h. The solid product obtained after the reaction was separated by filtration and washed with distilled water until the pH of the filtrate reached 7, ensuring the absence of hydroxide ions and impurities. The product was then dried at 80 °C for 24 h. Finally, during the calcination process in a furnace to remove the organic template and facilitate pore formation, the temperature was raised from room temperature to 550 °C at a heating rate of 1 °C/min and maintained at this temperature for 6 h,. The same procedure was followed to create the remaining metal catalysts, varying the amounts of metal salts while maintaining the silica source and template quantity constant.

2.3. Catalyst characterization

2.3.1. N_2-adsorption (BET)
N_2 adsorption-desorption studies were carried out after the samples had been degassed for 2 h at 393.15 K. Isotherms were obtained in a Micromeritics ASAP Instrument, and the corresponding specific areas were determined by the Brunauer-Emmett-Teller (BET) method.

2.3.2. FT-IR
The calcined samples underwent analysis through a Fourier transform infrared (FT-IR) spectroscopy instrument manufactured by JASCO with the model (FT-IR 4100), which covers the wavenumber range of 4000-400 cm^{-1} for consistency in the scan range. Spectroscopic grade potassium bromide (KBr) was used as the medium, and the collected data underwent further analysis.

2.3.3. XRD
X-ray diffraction patterns of the samples were captured using a Philips PW1730 XRD instrument equipped with Cu K_α radiation. The measurements were performed over a scanning range of 0.8°–10° with a precise 2θ step size of 0.05 per second. The experiments were performed at a controlled temperature of 25 °C. The X-ray generator was set at 0 kV and 0 mA for all measurements to ensure accuracy and comparability. To avoid any problems with lighting when measuring low 2θ angles, we used a standardized sample holder to ensure that the samples were always positioned consistently.

2.3.4. SEM-EDX
The surface morphology of the samples and the elemental composition of the catalysts were examined using a MIRA3 TESCAN-LMU scanning electron microscope (SEM) equipped with an Energy-dispersive X-ray spectrometer (EDX) operating at an accelerating voltage of 20 kV.

2.4. Oxidative glucose experiment using V–Mo-MCM-41 (34)

The experiment was conducted in a 250 ml Erlenmeyer flask equipped with a rubber stopper fitted with a tube to release NO_2 gas, as shown in Fig. 1. The experiments were generally carried out as follows.

Initially, the required amount of molasses was added to the Erlenmeyer flask and heated to the reaction temperature (65 °C) while stirring with a magnetic stirrer. Once the desired reaction temperature was reached, the specified amount of nitric acid was added, followed by gradually adding the required amount of sulfuric acid to the reaction mixture while continuing the stirring. Finally, the
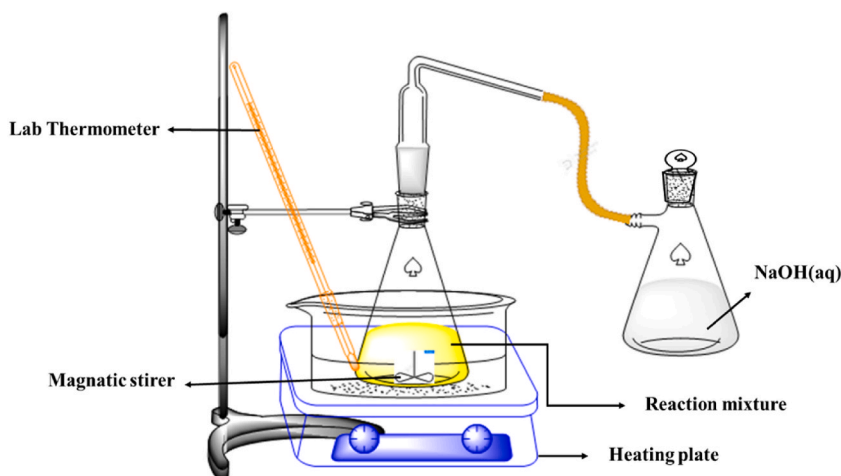

Fig (1). Experimental setup.

desired amount of the prepared nanocatalyst V–Mo-MCM-41 (34) was added to the reaction mixture, and the reaction temperature was maintained constant while vigorous stirring was continued throughout the reaction period.

After completing the reaction time, the nanocatalyst was filtered out, and then approximately half of the resulting solution was evaporated. The solution was then cooled to 5 °C for the crystallization process. The formed oxalic acid hydrate crystals were separated by filtration and dried at 50 °C. Approximately 60 % of the resulting filtrate from the first evaporation was evaporated, and the solution was cooled again to 5 °C. The formed crystals were separated by filtration and dried. The yield of oxalic acid was calculated by dividing the weight of the obtained oxalic acid by the theoretical weight of oxalic acid:

Yield = (Weight of obtained oxalic acid/Theoretical weight of oxalic acid)*100.

The theoretical weight of oxalic acid was calculated using the following chemical equation.

The emitted nitrogen oxides (such as NO and NO_2) are absorbed into a sodium hydroxide solution in another chamber to avoid atmospheric pollution and utilize the resulting gases to produce useful chemicals. The chambers are connected using rubber pipes. The absorption reaction occurs when the emitted nitrogen oxides react with the sodium hydroxide solution, forming sodium nitrite according to the following reaction [60,63,64].

Sodium nitrate has various applications; it is used as a low-cost fertilizer and serves as an additive to prevent the expansion of bacteria and fungi in packaged foods, pharmaceuticals, and other related products [64,68].

2.5. Response surface methodology

Response surface methodology (RSM) is a comprehensive experimental design and mathematical modeling approach that can be used to understand the relationship between operational factors and improve various industrial processes. One of the most commonly used designs is the Central Composite Design (CCD), the Fractional Factorial Design, with a central point connected to a set of axial points. The CCD can be represented as a square (for a two-factor design) or a cube (for a three-factor design), with vertices representing the low and high levels, denoted as −1 and +1, respectively [69].

The effectiveness of four vital operating factors, including catalyst dosage (X_1), sulfuric acid quantity (X_2), nitric acid quantity (X_3), and reaction time (X_4), was systematically evaluated using the CCD. Each independent variable was tested at five levels, including - α, −1, 0, +1, and + α, for low axial levels, low and central factors, and high factors and high axial levels, respectively. The encoded levels of the selected variables are summarized in Table 1. The total number of required experimental runs (N) can be calculated using Eq (1):

$$N = 2^n + 2n + n_c \tag{1}$$

Here, n, n_c refer to the variable number and the number of repetitions for the central point, respectively. For statistical analyses and optimization of each operation, a quadratic model was selected as the best-fit model and fitted to the results according to Eq (2) [70, 71]:

$$Y = \beta_0 + \sum_{i=1}^{k} \beta_i X_i + \sum_{i=1}^{k} \beta_{ii} X_i^2 + \sum_{i<j} \beta_{ij} X_i X_j + \varepsilon \tag{2}$$

Where Y is the expected response predicted by RSM, i and j are the linear and quadratic terms, respectively, β is the regression coefficient, k is the number of factors studied and optimized in the experiment, and ε represents the random error.

3. Results and discussion

3.1. N_2 adsorption (BET)

The porous characteristics of the prepared V–Mo-MCM-41 nanocatalysts, such as specific surface area, pore diameter, and pore volume, were determined by conducting physical adsorption measurements using nitrogen gas [72]. Nitrogen isotherms (adsorption-desorption) were obtained by subjecting the catalysts to liquid nitrogen at 77 K, as illustrated in Fig. 2. These isotherms represent the changes in the amount of nitrogen gas adsorbed on the catalyst surface (1g) at relative pressure (p/p_0) under constant temperature. The observed isotherm shapes belong to type IV, a characteristic feature of mesoporous materials according to the classification defined by the International Union of Pure and Applied Chemistry (IUPAC) [73]. A key feature of Type IV isotherms is that capillary condensation is accompanied by a slowdown, which initiates when the pore diameter exceeds 4 nm. This is evident in catalysts prepared with pore diameters larger than 4 nm, explaining the absence of a hysteresis loop in the sample (Si/V + Mo = 85) with a pore

Table 1
The levels and ranges of the independent variables applied in the central composite design.

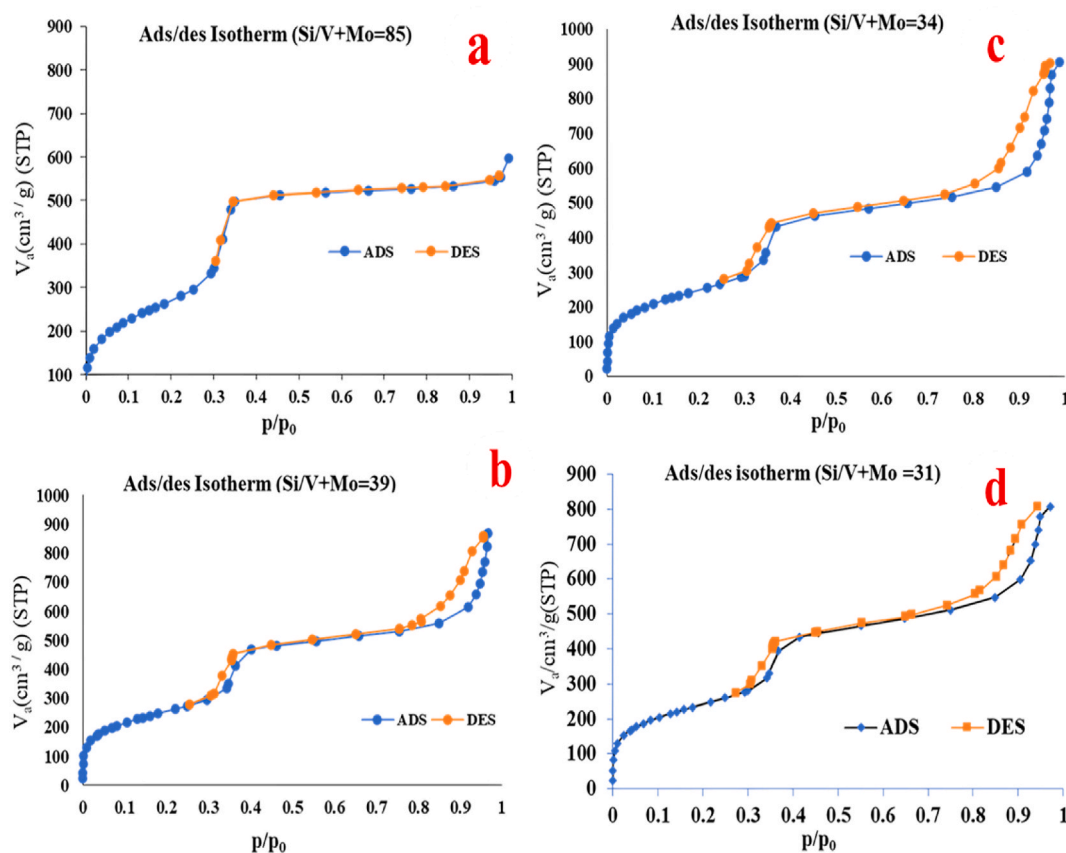| Factors	Unit	-α	−1	0	+1	+α
Catalyst dosage	gr	0.03125	0.0375	0.04375	0.05	0.05625
Sulfuric acid	ml	1.5	2	2.5	3	3.5
Nitric acid	ml	23.75	25	26.25	27.5	28.75
Time reaction	min	37.5	45	52.5	60	67.5

Fig (2). N_2-adsorption isotherms of calcined V–Mo-MCM-41 samples: Si/V + Mo = 85(a), Si/V + Mo = 39(b), Si/V + Mo = 34(c) and Si/V + Mo = 31(d).

diameter less than 4 nm [74–76].

The adsorption stages in the type IV isotherm exhibit variations depending on the applied gas pressure. In the initial stage, adsorption occurs on the catalyst surface (external or internal) at low relative pressures below ($P/P_0 = 0.2$). A slow linear increase in nitrogen adsorption characterizes it. This indicates the presence of monolayer to multilayer adsorption on the pore walls. The adsorption data in this stage can be used to calculate the specific surface area using the BET method. In the second stage, multilayer adsorption occurs at higher relative pressures, accompanied by a distinct step between ($p/p_0 = 0.28$ and 0.34), as depicted in Fig. 2. This sharp step indicates the occurrence of capillary condensation within the pores due to the filling of pores with liquid nitrogen. A characteristic feature of mesoporous materials. This signifies the filling of mesopores, with no pore filling observed at low pressures. The magnitude of this jump (the step) reflects the regularity and distribution of pore sizes. It correlates with the Kelvin equation linking pore diameter to the relative pressure at which capillary condensation occurs. In the third and final stage, a second step appears at higher relative pressures ($P/P_0 > 0.84$), signifying the filling of larger pores. This stage is characterized by a notable rise in nitrogen gas adsorption, reaching saturation pressure at ($P/P_0 = 1$). A plateau at high relative pressures is associated with multilayer adsorption on the external surface. The presence of some large pores in the samples suggests the existence of a hysteresis loop at high relative pressures [23,75,77–79].

Table 2 shows how varying quantities of vanadium and molybdenum affect the specific surface area, pore volume, and diameter. This variation indicates the drop in specific surface areas with increasing integrated metal content, followed by a slight increase in specific surface areas in the sample (34) and a decrease in the sample (31).

As the concentration of integrated metals increases due to the substitution of silicon ions with vanadium or molybdenum ions, we

Table 2
N_2 adsorption data results of V-M0-MCM-41 samples and (V + Mo) contents.

Catalyst	V + Mo%	S_{BET}	$D_p(nm)$	$V(cm^3/g)$
V–Mo-MCM-41(85)	0.62	955.37	3.8399	0.9119
V–Mo-MCM-41(39)	1.24	875.59	6.3862	1.3988
V–Mo-MCM-41(34)	1.57	900.33	5.9667	1.2575
V–Mo-MCM-41(31)	1.79	854.28	5.8514	1.2467

see a decrease in pore volume and pore diameter from sample (39) to sample (31), resulting in a longer (Si–*O*-M) bond than (Si–*O*–Si) bond caused by larger metal ions diameter [24,47]. As a result, the process of metal incorporation into the MCM-41 structure substantially impacts pore properties while keeping some of the mesoporous structure.

The irregular variation in samples (34) and (85) is presumably due to the non-crystalline structure of MCM-41.

Where S_{BET} is the Surface Area (m^2/g), D_p is the Average pore Diameter (nm), and V is the pore Volume (cm^3/g).

3.2. FT-IR

Infrared (IR) spectra were obtained for variously produced nanocatalysts (V–Mo-MCM-41) with varied vanadium and molybdenum ratios and the MCM-41 material. The resulting absorption spectrums are depicted in Fig. 3, which show a discrete absorption band at 963 cm^{-1} attributable to the vibrational mode of the (Si–*O*-M) bond, suggesting the incorporation of a heterogeneous atom into the MCM-41 structure where (M = V, Mo). Surprisingly, this band does not appear in the MCM-41 spectrum.

The band seen at (3450 cm^{-1}) suggests asymmetric stretching of the surface silanol group (Si–OH) and its associated water molecules. Similarly, the band at (1635 cm^{-1}) reflects a water molecule bending vibration (H–OH). Furthermore, the bands seen at (1081 and 804 cm^{-1}) correspond to the siloxane bond's symmetric and asymmetric stretching vibrations (Si–*O*–Si). Similarly, the band (456 cm^{-1}) exhibits a bending vibration of the siloxane bond (Si–*O*–Si) [38,80–82].

3.3. XRD

Despite the amorphous nature of MCM-41, it exhibits a regular hexagonal porous structure resembling a honeycomb, indicating the early stages of crystallization. Therefore, prepared catalysts can be characterized using X-ray diffraction (XRD). The XRD spectra show a distinct and sharp peak (d_{100}) at small angles ($2\theta = 1–10°$), along with weaker secondary peaks (d_{110}, d_{200}, d_{210}).

These secondary peaks represent long-range order in the material. The intensity of these secondary peaks decreases or even disappears when the samples are calcined at 550 °C or higher. Additionally, by adding up the metal content incorporated into the MCM-41 structure, the intensity of these secondary peaks declines or vanishes, indicating structural distortions caused by metal incorporation [24,72,83,84], In accordance with the references, it is noted that there is a singular peak, aligning with the observed data [70, 85,86].

It is evident that calcination and metal loading significantly impact the structural properties of V–Mo-MCM-41 catalysts. Calcination is believed to induce structural changes within the material, affecting the distribution and arrangement of elements at the crystalline network level. In this case, calcination may lead to the disappearance of secondary peaks. When incorporating metals into the MCM-41 structure, the chemical composition of the material is altered, influencing the distribution of metals within the crystalline network while maintaining prominent and sharp peaks (d100).

Fig. 4 and Table 3 show the patterns and XRD data of the prepared and calcined V–Mo-MCM-41 samples at 550 °C for 6 h, within the 2θ range of 1–10°. We observe from the figure the absence of secondary peaks (d110, d200, d210) as indicated in the reference studies, which are characteristic of pure MCM-41 material. This absence can be attributed to the reasons mentioned earlier in the prepared catalysts (V–Mo-MCM-41).

Revealing a prominent and robust peak (d_{100}) at $2\theta = 1°$ for samples with Si/V + Mo ratios of 85, 39, and 34. However, no peak is observed for the sample with a Si/V + Mo ratio of 31. Additionally, increasing metal content was observed with a fall in peak intensity and an increase in peak width at half maximum (FWHM).
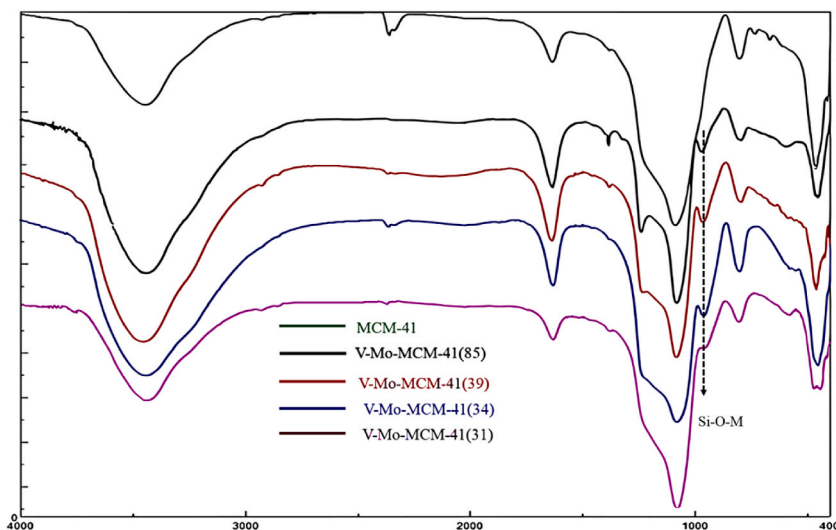

Fig (3). Presents the observed absorption bands in the spectrum and their corresponding wavenumbers.
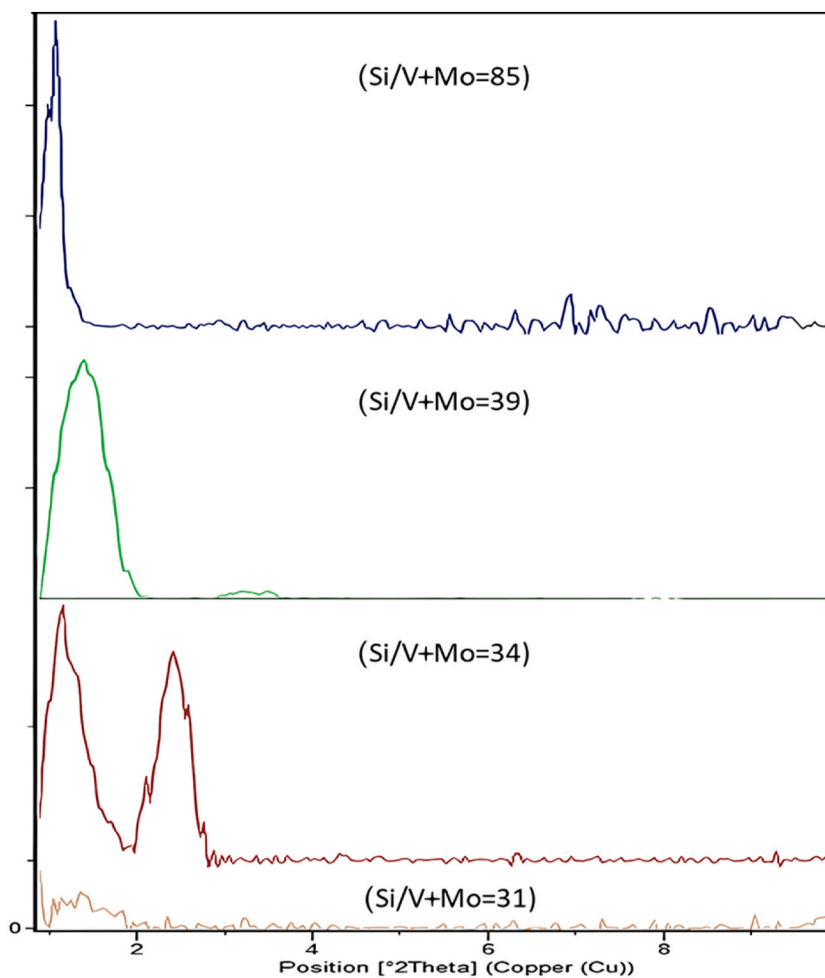
Fig (4). X-ray diffraction patterns of calcined V–Mo-MCM-41 sample.

Table (3)
Results of XRD data for V–Mo-MCM-41 samples.

Si/(V + Mo)	2 θ	FWHM	d spacing d₁₀₀ (nm)	α₀ (nm)	T (nm)
85	1.018	0.295	8.673776	10.015	6.17571
39	1.425	0.344	6.195899	7.154	0.7682
34	1.142	0.492	7.730171	8.926	2.9593

Where α_0 is the unit cell parameter $\left(\alpha_0 = \frac{2d_{100}}{\sqrt{3}}\right)$, and T is the wall thickness ($T = \alpha_0 - D_p$).

Subsequently, calculations were performed to determine the dimensions of the resulting crystals using Scherrer equation Eq (3) [87].

$$D = \frac{K\lambda}{\beta_{FWHM}.\cos(\theta)} \tag{3}$$

where (K) is a constant with a value of (0.94), the peak width at half maximum is measured in radians, and (D) represents the crystal dimensions in nanometers. Additionally, the strain density (δ) was calculated, which is defined as the distance between dislocation lines per unit volume of the crystal and is determined using Eq (4):

$$\delta = \frac{1}{D^2} \tag{4}$$

The internal strain (ε) is a defect that occurs during the crystallization process and is closely linked to the presence of different types

of crystal defects (point defects, surface defects, and volume defects) [87]. Its calculation was based on Eq (5) [88]:

$$\varepsilon = \beta_{FWHM} \frac{\cos(\theta)}{4} \tag{5}$$

Table 4 shows a drop in (D) value and a rise in (δ, ε) values as metal levels increase, attributable to structural distortions produced by metal incorporation, which caused the XRD peak in the (31) sample pattern to decline [89]. The calculated and measured values in Table 4 confirm the attainment of nanoscale dimensions.

3.4. SEM analysis

These microscopy results provide valuable insights into the nanoscale characteristics of the catalysts, reflecting the influence of metal content on their particle size and aggregation behavior.

Fig. 5 displays the prepared catalysts' scanning electron microscopy (SEM) images. The nanoscale dimensions are evident in all four samples, and there is a decrease in the size of the nanocrystals with increasing metal content, consistent with the XRD data obtained from the Scherrer equation. In sample (V–Mo-MCM-41 (85)), as shown in Fig. 5(a), most particles appear relatively large and singular, with dimensions ranging from 40 to 140 nm. In contrast, Fig. 5(b) of the catalyst (V–Mo-MCM-41 (39)) reveals nanoparticles aggregating in clusters, with dimensions ranging from 25 to 55 nm.

Moving on to sample (V–Mo-MCM-41 (34)) in Fig. 5(c), it exhibits smaller particle size within the range of 25–70 nm compared to the previous catalysts. The particles have a more regular spherical shape and aggregate in nanoclusters. The same observation applies to sample (V–Mo-MCM-41 (31)) in Fig. 5(d), where a decrease in particle size is noticeable.

3.5. EDX analysis

The EDX spectra of the prepared catalysts in Fig. 6(A-D) illustrate silicon, oxygen, vanadium, and molybdenum weight percentages. The obtained results indicate that oxygen and silicon are the primary elements in the structure of the prepared mesoporous nanoscale silica particles (MCM-41). In Fig. 6, a decrease in the Si/V + Mo ratio is observed in the prepared nanocatalysts with an increase in the loading ratio, indicating an enhanced dispersion of additional metals on the MCM-41 surface. As depicted in Fig. 6(A), the Si/V + Mo ratio is 85; in Fig. 6(B), it reduces to 39. Moving to Fig. 6(C), the Si/V + Mo ratio further decreases to 34, demonstrating an increase in the calcined nanocatalysts' total (V + Mo) content. Finally, in Fig. 6(D), the Si/V + Mo ratio reaches 31, representing the highest loading ratio. This signifies an elevated concentration of (V + Mo) in the nanocatalysts, highlighting the impact of loading on metal dispersion on the MCM-41 surface.

3.6. Central composite design

The synthesis of oxalic acid from molasses was enhanced using Central Composite Design (CCD). A total of 30 experiments were randomized based on the CCD design, using a V–Mo-MCM-41 (34) catalyst. The experimental data and results presented in Table 5 highlight the significant impact of the selected operational variables, their actual values, and the corresponding responses (predicted values). Utilizing the Response Surface Methodology (RSM), the effects of four key process factors, namely catalyst dosage (X_1), sulfuric acid quantity (X_2), nitric acid quantity (X_3), and reaction time (X_4), as well as their interactions, were thoroughly investigated. Then, the collected data was analyzed and fitted into a mathematical model eq (6).

$$Y = +75.67 + 1.17X_1 + 1.63X_2 + 2.58X_3 + 1.12X_4 - 3.08X_1X_2 - 0.2928X_1X_3 + 0.4164X_1X_4 + 0.3152X_2X_3 - 0.0500X_2X_4$$
$$- 0.0135X_3X_4 \tag{6}$$

This mathematical equation helped to analyze the connections between independent variables and dependent responses. It aimed to determine the optimal conditions for producing the highest amount of oxalic acid from molasses.

3.7. Statistical analysis and the model fitting

Table 6 contains the outcomes of the analysis of variance (ANOVA). The significant F-value of 105.59 suggests the importance of the model, with only a 0.01 % chance of such a large F-value occurring due to noise. The p-values less than 0.0500 indicate the significance of the selected model terms. Terms X_1, X_2, X_3, X_4, X_1X_2, and X_1X_4 are identified as notable model terms. On the other hand, values greater than 0.1000 imply that specific model terms are not statistically significant. The insignificant lack of fit F-value of 0.51

Table (4)
values of D, δ, ε for V–Mo-MCM-41 (85, 39, 34) samples.

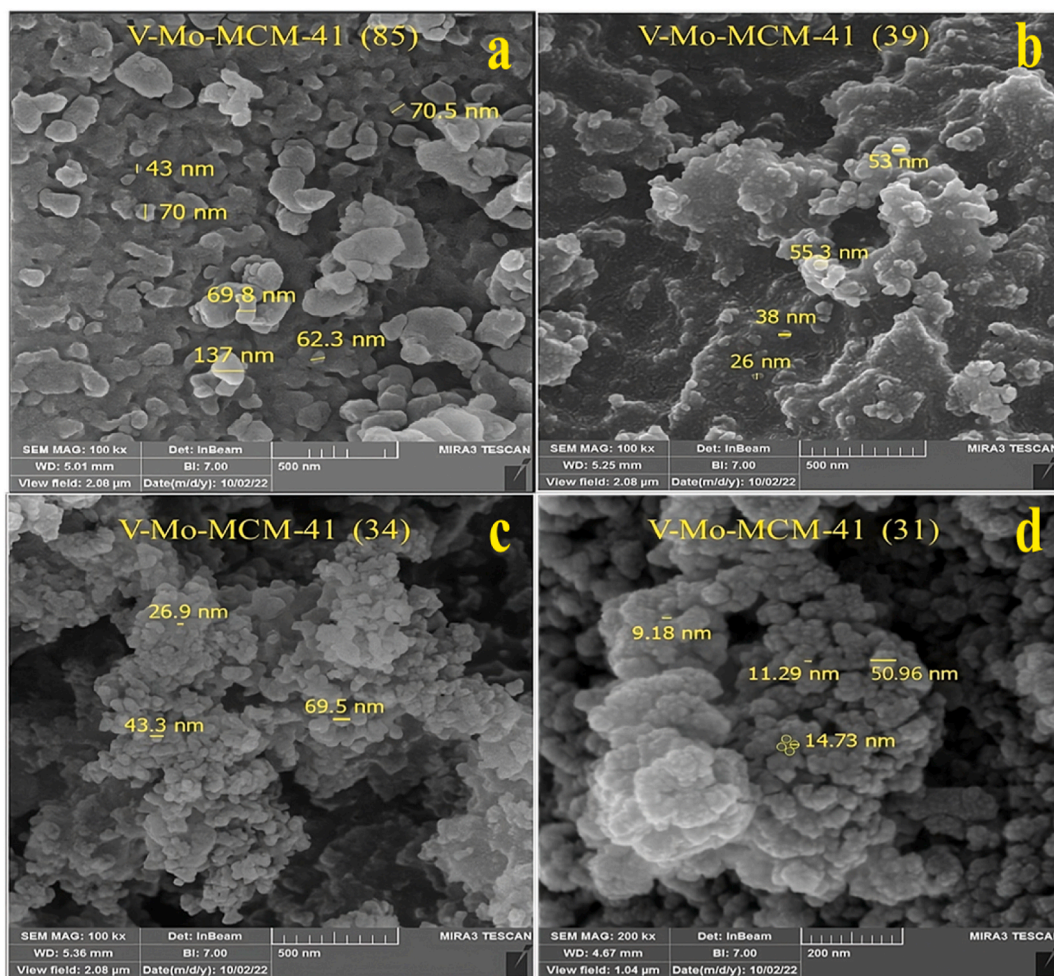| Si/(V + Mo)	V + Mo%	2θ	D(n)	δ	ε*1000
85	0.62	1.018519	28.10873	1.26566E+15	0.695981
39	1.24	1.425865	24.09411	1.72258E+15	0.812026
34	1.57	1.142851	16.86541	3.51565E+15	1.159987

Fig (5). SEM images for samples: Si/V + Mo = 85(a), Si/V + Mo = 39(b), Si/V + Mo = 34(c) and Si/V + Mo = 31(d).

indicates that lack of fit is not a significant factor in pure error. There is an 85.57 % chance that such a lack of fit could happen due to noise. It is favorable to have a slight lack of fit.

The high R-squared value of 0.9823 for glucose oxidation indicates that the proposed model reasonably fits the experimental data. The expected R-squared value of 0.9671 reasonably agrees with the adjusted R-squared value of 0.9730, with a difference of less than 0.2. Fig. 7 compares the experimental data conducted in the laboratory and the predicted values for oxalic acid yield. Adeq Precision, which measures the signal-to-noise ratio, exceeds the desired threshold of 4 with a value of 42.189, indicating a sufficient signal. This model can be effectively used to explore the design space.

The small coefficient of variation (C.V. %) value of 0.8568 indicates a high degree of precision in comparing the experiments, where lower C.V. values imply greater reliability. The standard deviation (Std. Dev.) of 0.6484 indicates good reliability. Based on the small predicted residual error sum of squares (PRESS) value of 14.87, the model can fit each data point well. A smaller PRESS value indicates a better fit for the data points [90].

The estimated coefficient represents the expected change in the response for each unit change in the factor value while keeping all other remaining factors constant. The effects of the significant variables were indicated by positive and negative signs of the variable coefficients within the proposed model equation [91]. By examining the variable coefficients in this model equation, four independent variables (X_1, X_2, X_3, and X_4) showed primary significance with a positive effect on the response. Fig. 8 illustrates the main effects of these factors on oxalic acid productivity at the central point of the other variables.

3.8. Response surface plots

To investigate the impact of different factors on oxalic acid production and determine the optimal values for these factors, a three-dimensional (3D) response surface was plotted in Figure (8), which provides insights into oxalic acid production. Fig. 8(a) shows that nitric acid quantity and reaction time were kept constant at the central points (26.25 ml, 52.5 min). It illustrates that increasing the sulfuric acid and decreasing the catalyst quantity led to an improved yield. Furthermore, the contour plot Fig. 8(b) associated with
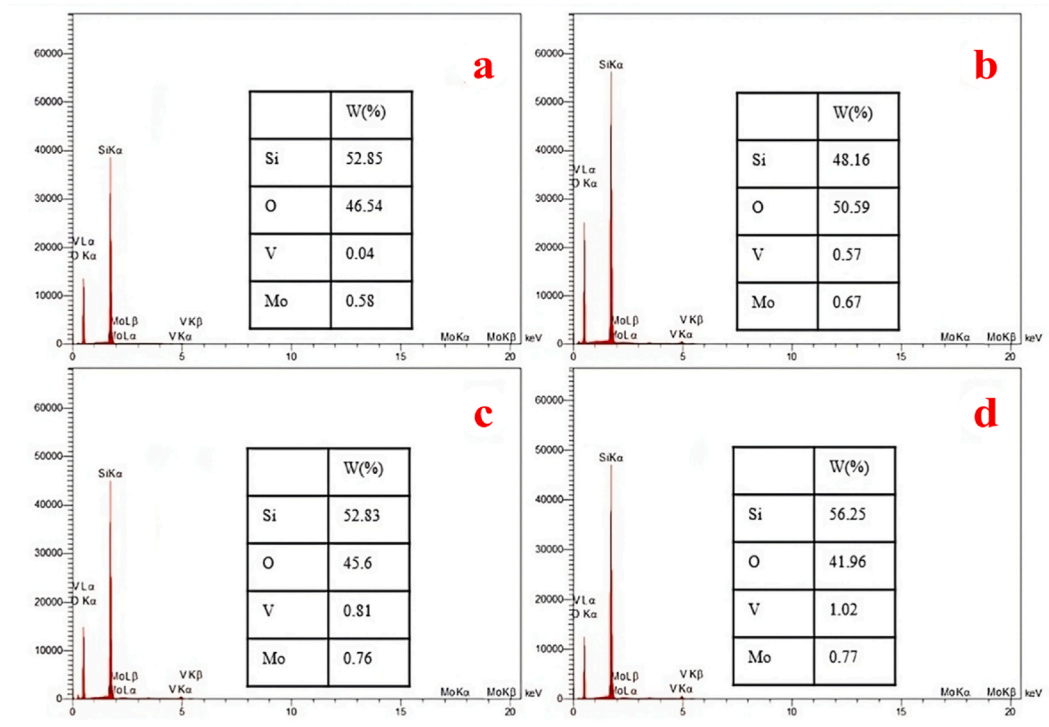
Fig (6). EDX Spectra for samples: Si/V + Mo = 85(a), Si/V + Mo = 39(b), Si/V + Mo = 34(c) and Si/V + Mo = 31(d).

Table (5)
Data for experimental and predicted oxalic acid yield.

Run	Factor 1	Factor 2	Factor 3	Factor 4	Response 1	Response 2
	X_1: Catalyst dosage (gr)	X_2: Sulfuric acid (ml)	X_3: Nitric acid (ml)	X4: Time reaction (min)	Experimental (%)	Predicted (%)
1	0.04375	2.5	26.25	52.5	75.1436	75.6752
2	0.05	3	25	45	71.2807	71.3069
3	0.0375	3	27.5	60	82.9721	83.0353
4	0.04375	2.5	26.25	37.5	73.1206	73.4434
5	0.04375	2.5	26.25	52.5	76.3424	75.6752
6	0.0375	3	25	45	75.2879	75.3648
7	0.04375	3.5	26.25	52.5	79.1147	78.9413
8	0.05	3	25	60	74.3194	74.2985
9	0.05	2	25	45	74.9954	74.7291
10	0.05	2	27.5	60	82.1132	81.8331
11	0.04375	2.5	26.25	52.5	76.2314	75.6752
12	0.05	2	25	60	77.9378	77.9206
13	0.03125	2.5	26.25	52.5	73.1521	73.328
14	0.0375	3	27.5	45	81.851	81.7633
15	0.0375	3	25	60	76.7792	76.6909
16	0.0375	2	27.5	45	71.7913	71.609
17	0.04375	2.5	26.25	52.5	75.1139	75.6752
18	0.0375	2	25	60	67.8923	67.9973
19	0.04375	2.5	23.75	52.5	71.6664	70.5197
20	0.04375	2.5	26.25	52.5	74.2528	75.6752
21	0.0375	2	27.5	60	73.212	73.0809
22	0.04375	2.5	28.75	52.5	81.0101	80.8307
23	0.05	3	27.5	45	76.8425	76.5343
24	0.05	3	27.5	60	80.1122	79.4718
25	0.04375	2.5	26.25	67.5	77.1898	77.9069
26	0.05	2	27.5	45	78.7124	78.6957
27	0.04375	2.5	26.25	52.5	75.9828	75.6752
28	0.04375	1.5	26.25	52.5	72.9454	72.4091
29	0.05625	2.5	26.25	52.5	76.9391	78.0223
30	0.0375	2	25	45	65.9359	66.4713

Table (6)
Analysis of variance (ANOVA) for oxidative glucose.

| Source	Sum of Squares	df	Mean Square	F-value	p-value	
Model	443.87	10	44.39	105.59	<0.0001	significant
X_1- Catalyst dosage	33.05	1	33.05	78.63	<0.0001	
X_2-Sulfuric acid	64.00	1	64.00	152.25	<0.0001	
X_3-Nitric acid	159.47	1	159.47	379.35	<0.0001	
X_4-Time reaction	29.88	1	29.88	71.08	<0.0001	
X_1X_2	151.68	1	151.68	360.80	<0.0001	
X_1X_3	1.37	1	1.37	3.26	0.0868	
X_1X_4	2.77	1	2.77	6.60	0.0188	
X_2X_3	1.59	1	1.59	3.78	0.0668	
X_2X4	0.0400	1	0.0400	0.0950	0.7612	
X_3X_4	0.0029	1	0.0029	0.0070	0.9343	
Residual	7.99	19	0.4204			
Lack of Fit	4.68	14	0.3342	0.5051	0.8557	not significant
Pure Error	3.31	5	0.6617			
Cor Total	451.85	29				
Std. Dev.	0.6484		**R^2**	0.9823		
Mean	75.67		**Adjusted R^2**	0.9730		
C.V. %	0.8568		**Predicted R^2**	0.9671		
			Adeq Precision	42.1891		
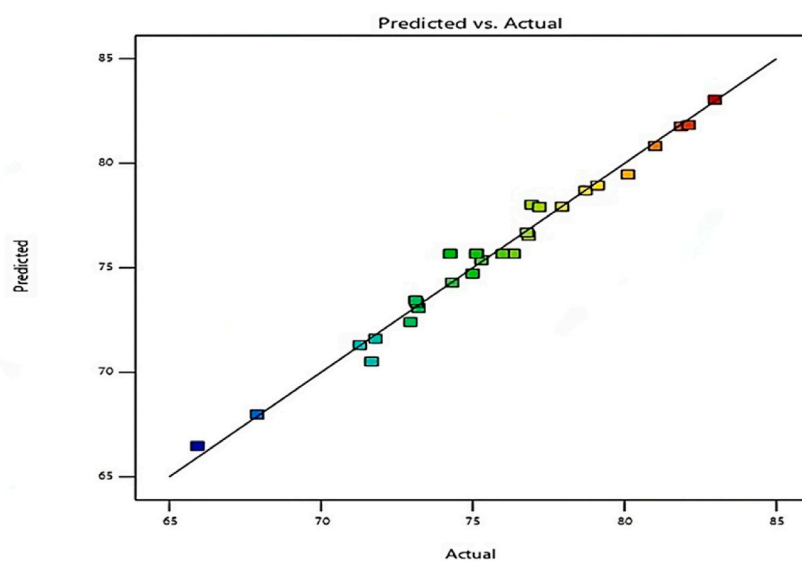
Fig (7). Comparison of the experimental results of oxalic acid conversion with those calculated via the CCD equation.

these variables demonstrated a significant interaction, indicating the effective influence of these factors on oxalic acid production. Notably, sulfuric acid had a more substantial impact on yield when the catalyst dosage was low, as supported by the higher coefficient estimate for the response to sulfuric acid (1.63) compared to the response to catalyst dosage (1.17), as shown in Eq (6).

Fig. 8(c) highlights the effects of catalyst dosage and reaction time on oxalic acid yield while keeping nitrogen acid and sulfuric acid quantities constant at (27.5 ml, 2 ml) respectively. The figure shows that increasing reaction time and catalyst dosage increases oxalic acid yield. Moreover, the contour plot in Fig. 8(d) reveals a notable interaction between the variables, underscoring the substantial influence of these factors on oxalic acid production. It is important to highlight that, as demonstrated by equation (6), the catalyst dosage exerts a slightly greater impact on the yield, particularly when the reaction time is extended. The response factor for catalyst dosage, at 1.17, surpasses that of reaction time, which stands at 1.12, underscoring the significance of the catalyst dosage in optimizing oxalic acid production.

3.9. Evaluation of the efficiency of the other catalysts

The performance of different prepared catalysts with varying compositions (Si/V + Mo = 85, 39, 31) was assessed to determine the most effective mesoporous nanocatalyst for glucose oxidation. To achieve this, the reaction was carried out using these catalysts at the central point of each factor, involving specific catalyst dosage (X_1 = 0.04375g), quantities of sulfuric acid (X_2 = 2.5 ml), and nitric acid
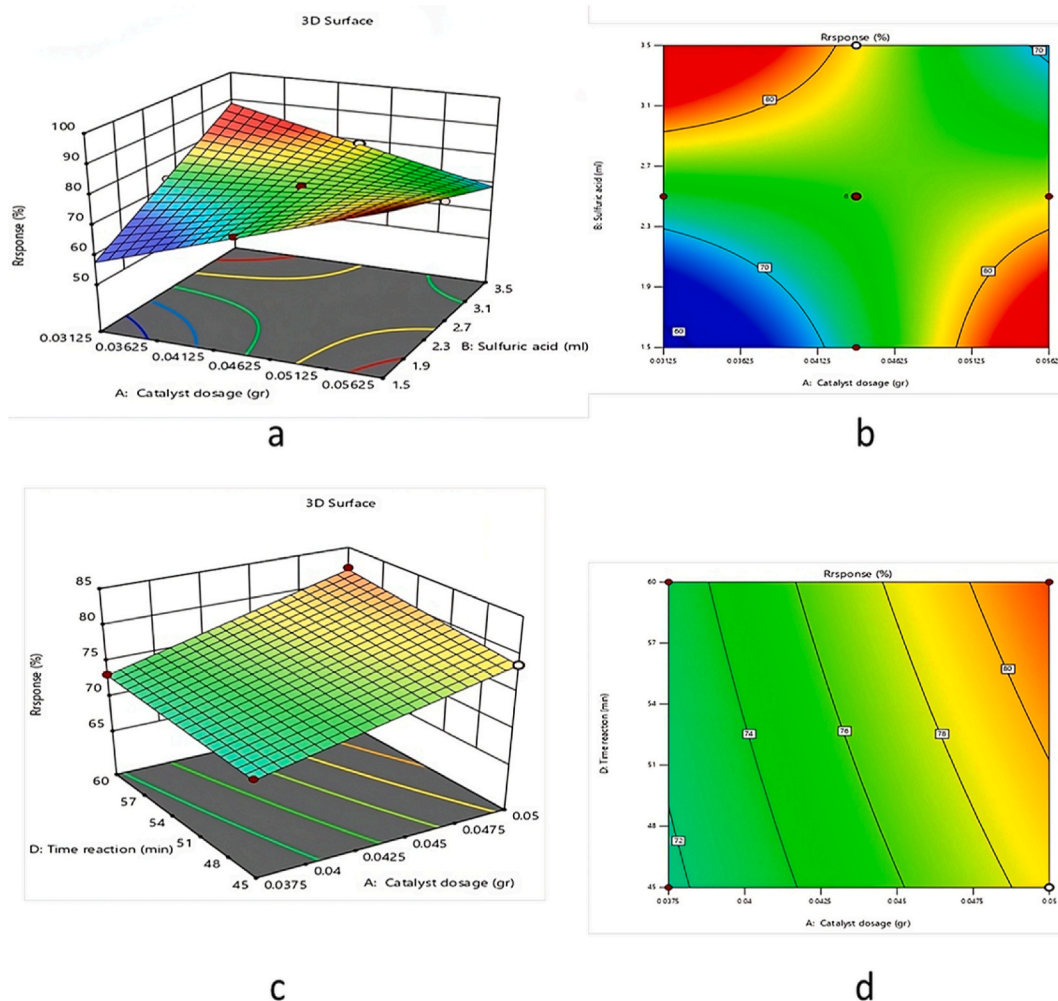
Fig (8). Response surface and contour plot for oxalic acid production as a function of (a,b) sulfuric acid amount and catalyst dosage, (c,d) reaction time and catalyst dosage.

($X_3 = 26.25$ ml), as well as reaction time ($X_4 = 52.5$min). The efficacy of the prepared catalysts was also compared to that of the V_2O_5 catalyst and the VK38 catalyst (6–8% V_2O_5).

Fig. 9 compares the performance of the prepared catalysts, the V_2O_5 catalyst, the VK38 catalyst (6–8% V_2O_5%), and the reaction conducted without a catalyst. The V–Mo-MCM-41 (34) catalyst stands out for its superior efficiency. Nonetheless, there's an observed decrease in yield to 80 % with the V–Mo-MCM-41 (31) catalyst, characterized by a higher loading ratio. This drop can be attributed to structural distortions in the catalyst, as evident from the XRD analysis results.

We observe an increase in catalytic activity with an increase in the quantity of vanadium and molybdenum incorporated into the structure of MCM-41. This is due to the decrease in particle size and the increase in Lewis acid sites on the catalyst surface, resulting from the complex species of supported vanadium and molybdenum oxides on the catalyst surface [47,49,50].

After conducting the application using the catalyst with a ratio of (Si/V + Mo = 34) and comparing the catalytic activity with the other prepared catalysts, we found that the catalyst containing the highest ratio of vanadium and molybdenum in the structure of MCM-41 and did not undergo structure degradation exhibited the highest effectiveness.

3.10. Catalyst reusability

The reusability of the catalyst is essential for industrial applications. The catalysts were recovered after separation, reactivated, and reused multiple times in the glucose oxidation reaction under the same conditions. A decrease in catalytic activity was observed in the fourth cycle, with an oxalic acid yield of 79.3 %. This decline could be attributed to blocking some active sites on the catalyst's surface, as shown in Fig. 10.

Fig. 11 illustrates the FT-IR spectrum of the catalyst after four consecutive reuse cycles and its subsequent regeneration through calcination to eliminate any organically deposited materials within the pores. From the spectrum, we observe no changes or
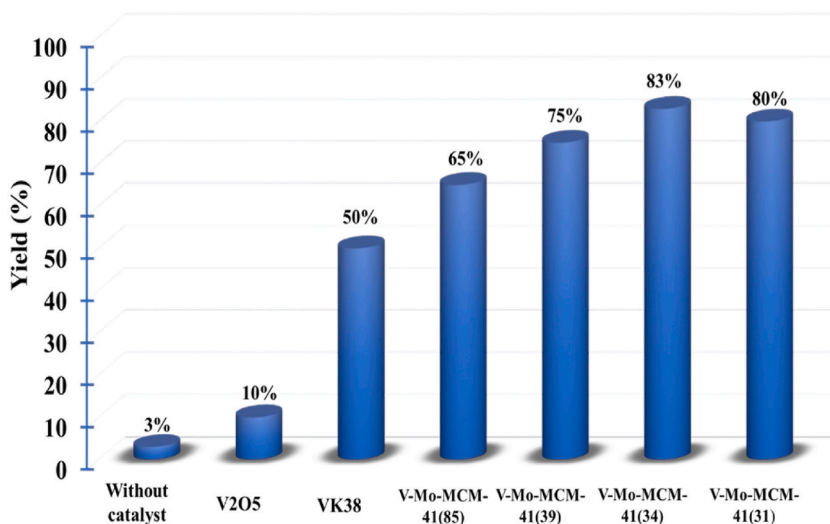
Fig (9). Catalysts performance, Reaction conditions: $X_1 = 0.04375$ g, $X_2 = 2.5$ ml, $X_3 = 26.25$ ml, $X_4 = 52.5$ min.

disappearance of bands corresponding to the metal (Si–*O*-M). This indicates the thermal and hydrothermal stability of the catalysts prepared in aqueous solutions during reactions.

4. Conclusion

This study, V–Mo-MCM-41 silicate-based nanocatalysts were synthesized using the hydrothermal direct method, employing different ratios (Si/V + Mo = 85, 39, 34, and 31). Spectroscopic analyses, including FT-IR and XRD, confirmed successful metal ion incorporation into the MCM-41 structure. This was evident through the appearance of a band at 963 cm^{-1}, accompanied by a reduction in the peak intensity of d100 and an increase in the peak width at half maximum (FWHM), indicative of structural distortion resulting from the integration of V and Mo metals. Nitrogen adsorption results revealed that the incorporation of metal ions significantly influenced specific surface area, pore diameter, and volume. The catalytic efficiency of the prepared nanocatalysts for oxalic acid production from molasses was evaluated using response surface methodology. The central composite design (CCD) was employed to investigate the impact of nitric acid, sulfuric acid, catalyst dosage, and reaction time on oxalic acid productivity and their interactions. All four factors demonstrated significant effects on yield, with nitric acid exhibiting the most substantial influence, as supported by the mathematical model equation.

Analysis of 3D response surface plots unveiled interactive effects between catalyst dosage and sulfuric acid quantity on oxalic acid yield, with the highest yield achieved at the maximum sulfuric acid amount and the minimum catalyst dosage. Additionally, the prepared catalysts exhibited heightened catalytic efficiency with an increased loading of vanadium and molybdenum.

In oxalic acid production, The synthesized catalysts outperformed V_2O_5 and VK38 (6–8% V_2O_5). This comprehensive study highlights the successful synthesis of V–Mo-MCM-41 nanocatalysts, elucidates their structural changes, and demonstrates their efficacy in oxalic acid production by systematically evaluating various factors. Furthermore, a critical comparison with prior catalysts
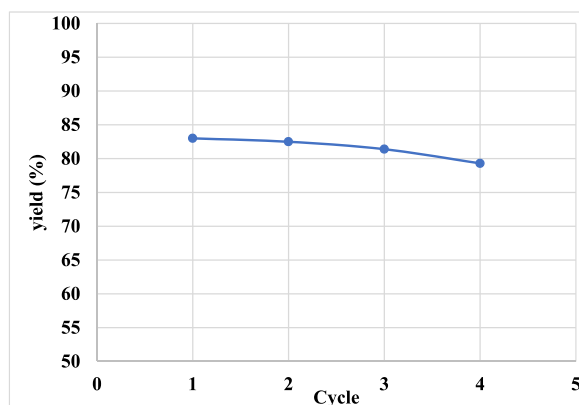
Fig(10). The effect of reusability on the yield.
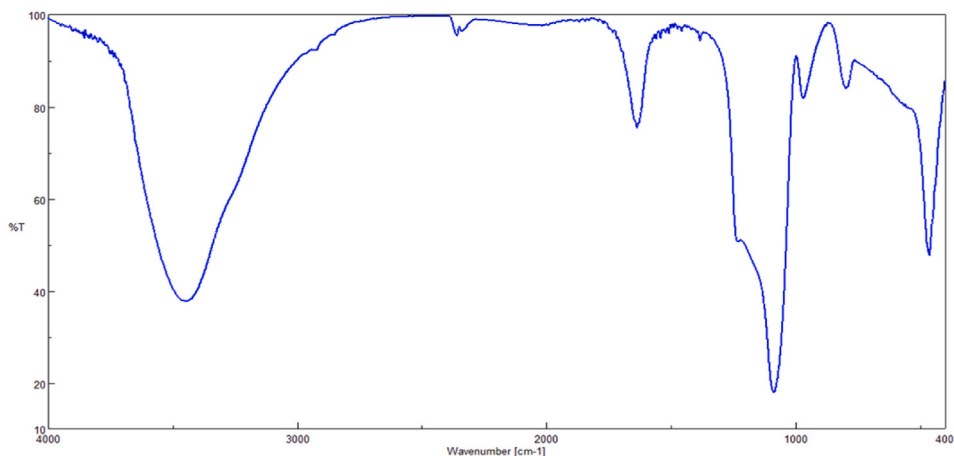
Fig(11). FT-IR of the catalyst after recycling of it for four times.

emphasizes integrating both vanadium and molybdenum metals into the MCM-41 framework for enhanced catalytic performance.

Additional information

No additional information is available for this paper.

Data availability statement

Data included in article/supp. material/referenced in article.

CRediT authorship contribution statement

Jasem Al Ebraheem: Writing – original draft, Visualization, Methodology, Investigation, Data curation, Conceptualization. **Mohammad Nour Alkhoder:** Supervision, Investigation, Data curation. **Reem Hani Tulaimat:** Writing – review & editing, Supervision, Data curation.

Declaration of competing interest

The authors declare that they have no known competing financial interests or personal relationships that could have appeared to influence the work reported in this paper.

References

[1] V. Polshettiwar, T. Asefa, Introduction to nanocatalysis, in: Nanocatalysis Synth. Appl., John Wiley & Sons, Inc., Hoboken, NJ, USA, 2013, pp. 1–9, https://doi.org/10.1002/9781118609811.ch1.
[2] S.-V. Berlin, H. Gmbh, Basic Principles in Applied Catalysis, Springer Berlin Heidelberg, Berlin, Heidelberg, 2004, https://doi.org/10.1007/978-3-662-05981-4.
[3] A. Taguchi, F. Schüth, Ordered mesoporous materials in catalysis, Microporous Mesoporous Mater. 77 (2005) 1–45, https://doi.org/10.1016/j.micromeso.2004.06.030.
[4] J.W. Niemantsverdriet, R. Schlögl, Heterogeneous catalysis: introduction, in: Compr. Inorg. Chem. II, Elsevier, 2013, pp. 1–6, https://doi.org/10.1016/B978-0-08-097774-4.00701-4.
[5] T. Armbruster, M.E. Gunter, Crystal structures of natural zeolites, Rev. Mineral. Geochem. 45 (2001) 1–67, https://doi.org/10.2138/rmg.2001.45.1.
[6] J. Weitkamp, Zeolites and catalysis, Solid State Ionics 131 (2000) 175–188, https://doi.org/10.1016/S0167-2738(00)00632-9.
[7] M.S. Morey, A. Davidson, G.D. Stucky, Silica-based, cubic mesostructures: synthesis, characterization and relevance for catalysis, J. Porous Mater. 5 (1998) 195–204, https://doi.org/10.1023/a:1009626103498.

[8] G. Øye, W.R. Glomm, T. Vrålstad, S. Volden, H. Magnusson, M. Stöcker, J. Sjöblom, Synthesis, functionalisation and characterisation of mesoporous materials and sol–gel glasses for applications in catalysis, adsorption and photonics, Adv. Colloid Interface Sci. 123 (126) (2006) 17–32, https://doi.org/10.1016/j.cis.2006.05.010.

[9] B. Chakraborty, B. Viswanathan, Surface acidity of MCM-41 by in situ IR studies of pyridine adsorption, Catal. Today 49 (1999) 253–260, https://doi.org/10.1016/S0920-5861(98)00431-3.

[10] G. Martínez-Edo, A. Balmori, I. Pontón, A.M. Del Rio, D. Sánchez-García, Functionalized ordered mesoporous silicas (MCM-41): synthesis and applications in catalysis, Catalysts 8 (2018), https://doi.org/10.3390/catal8120617.

[11] R.A. Curtis, M.W. Deem, A statistical mechanics study of ring size, ring shape, and the relation to pores found in zeolites, J. Phys. Chem. B 107 (2003) 8612–8620, https://doi.org/10.1021/jp027447+.

[12] J.S. Beck, J.C. Vartuli, W.J. Roth, M.E. Leonowicz, C.T. Kresge, K.D. Schmitt, C.T.W. Chu, D.H. Olson, E.W. Sheppard, S.B. McCullen, J.B. Higgins, J.L. Schlenker, A new family of mesoporous molecular sieves prepared with liquid crystal templates, J. Am. Chem. Soc. 114 (1992) 10834–10843, https://doi.org/10.1021/ja00053a020.

[13] G. Øye, J. Sjöblom, M. Stöcker, Synthesis, characterization and potential applications of new materials in the mesoporous range, Adv. Colloid Interface Sci. 89–90 (2001) 439–466, https://doi.org/10.1016/S0001-8686(00)00066-X.

[14] C.C. Freyhardt, M. Tsapatsis, R.F. Lobo, K.J. Balkus, M.E. Davis, A high-silica zeolite with a 14-tetrahedral-atom pore opening, Nature 381 (1996) 295–298, https://doi.org/10.1038/381295a0.

[15] T. Yanagisawa, T. Shimizu, K. Kuroda, C. Kato, The preparation of alkyltrimethylammonium–kanemite complexes and their conversion to microporous materials, Bull. Chem. Soc. Jpn. 63 (1990) 988–992, https://doi.org/10.1246/bcsj.63.988.

[16] A. Corma, From microporous to mesoporous molecular sieve materials and their use in catalysis, Chem. Rev. 97 (1997) 2373–2420, https://doi.org/10.1021/cr960406n.

[17] C.-Y. Chen, H.-X. Li, M.E. Davis, Studies on mesoporous materials, Microporous Mater. 2 (1993) 17–26, https://doi.org/10.1016/0927-6513(93)80058-3.

[18] J.L. Blin, G. Herrier, C. Otjacques, B.L. Su, Synthesis and Characterization of Ordered Mesoporous MCM-41 Materials, Elsevier Masson SAS, 2000, https://doi.org/10.1016/s0167-2991(00)80031-2.

[19] M.W. Maddox, J.P. Olivier, K.E. Gubbins, Characterization of MCM-41 using molecular simulation: heterogeneity effects, Langmuir 13 (1997) 1737–1745, https://doi.org/10.1021/la961068o.

[20] M. Kruk, M. Jaroniec, J.M. Kim, R. Ryoo, Characterization of highly ordered MCM-41 silicas using X-ray diffraction and nitrogen adsorption, Langmuir 15 (1999) 5279–5284, https://doi.org/10.1021/la990179v.

[21] S.B. Bukallah, A. Bumajdad, K.M.S. Khalil, M.I. Zaki, Characterization of mesoporous VOx/MCM-41 composite materials obtained via post-synthesis impregnation, Appl. Surf. Sci. 256 (2010) 6179–6185, https://doi.org/10.1016/j.apsusc.2010.03.137.

[22] H. Chen, Y. Wang, Preparation of MCM-41 with high thermal stability and complementary textural porosity, Ceram. Int. 28 (2002) 541–547, https://doi.org/10.1016/S0272-8842(02)00007-X.

[23] W.J. Kim, J.C. Yoo, D.T. Hayhurst, Synthesis of hydrothermally stable MCM-41 with initial adjustment of pH and direct addition of NaF, Microporous Mesoporous Mater. 39 (2000) 177–186, https://doi.org/10.1016/S1387-1811(00)00194-3.

[24] D. Lee, T. Liu, Characterization of V-MCM-41 mesoporous materials, J. Sol. Gel Sci. Technol. 24 (2002) 69–80, https://doi.org/10.1023/A:1015165600804.

[25] F.J. Méndez, A. Llanos, M. Echeverría, R. Jáuregui, Y. Villasana, Y. Díaz, G. Liendo-Polanco, M.A. Ramos-García, T. Zoltan, J.L. Brito, Mesoporous catalysts based on Keggin-type heteropolyacids supported on MCM-41 and their application in thiophene hydrodesulfurization, Fuel 110 (2013) 249–258, https://doi.org/10.1016/j.fuel.2012.11.021.

[26] D. Lu, S. Xu, W. Qiu, Y. Sun, X. Liu, J. Yang, J. Ma, Adsorption and desorption behaviors of antibiotic ciprofloxacin on functionalized spherical MCM-41 for water treatment, J. Clean. Prod. 264 (2020) 121644, https://doi.org/10.1016/j.jclepro.2020.121644.

[27] M. Brankovic, A. Zarubica, T. Andjelkovic, D. Andjelkovic, Mesoporous silica (MCM-41): synthesis/modification, characterization and removal of selected organic micro-pollutants from water, Adv. Met. Technol. 6 (2017) 50–57, https://doi.org/10.5937/savteh1701050B.

[28] P.A. Mangrulkar, S.P. Kamble, J. Meshram, S.S. Rayalu, Adsorption of phenol and o-chlorophenol by mesoporous MCM-41, J. Hazard Mater. 160 (2008) 414–421, https://doi.org/10.1016/j.jhazmat.2008.03.013.

[29] R.A.A. Melo, M.V. Giotto, J. Rocha, E.A. Urquieta-González, MCM-41 ordered mesoporous molecular sieves synthesis and characterization, Mater. Res. 2 (1999) 173–179, https://doi.org/10.1590/S1516-14391999000300010.

[30] T. Popova, B. Tzankov, C. Voycheva, I. Spassova, D. Kovacheva, S. Tzankov, D. Aluani, V. Tzankova, N. Lambov, Mesoporous silica MCM-41 and HMS as advanced drug delivery carriers for bicalutamide, J. Drug Deliv. Sci. Technol. 62 (2021) 102340, https://doi.org/10.1016/j.jddst.2021.102340.

[31] M. Manzano, V. Aina, C.O. Areán, F. Balas, V. Cauda, M. Colilla, M.R. Delgado, M. Vallet-Regí, Studies on MCM-41 mesoporous silica for drug delivery: effect of particle morphology and amine functionalization, Chem. Eng. J. 137 (2008) 30–37, https://doi.org/10.1016/j.cej.2007.07.078.

[32] A.K. Singh, S. Sen Singh, A.S. Rathore, S.P. Singh, G. Mishra, R. Awasthi, S.K. Mishra, V. Gautam, S.K. Singh, Lipid-coated MCM-41 mesoporous silica nanoparticles loaded with berberine improved inhibition of acetylcholine esterase and amyloid formation, ACS Biomater. Sci. Eng. 7 (2021) 3737–3753, https://doi.org/10.1021/acsbiomaterials.1c00514.

[33] J. Zhao, Y. Zhang, L. Xu, F. Tian, T. Hu, C. Meng, Weak base favoring the synthesis of highly ordered V-MCM-41 with well-dispersed vanadium and the catalytic performances on selective oxidation of benzyl alcohol, Chin. J. Chem. Eng. 28 (2020) 1424–1435, https://doi.org/10.1016/j.cjche.2020.02.027.

[34] L. Brahmi, T. Ali-Dahmane, R. Hamacha, S. Hacini, Catalytic performance of Al-MCM-41 catalyst for the allylation of aromatic aldehydes with allyltrimethylsilane: comparison with TiCl4 as Lewis acid, J. Mol. Catal. Chem. 423 (2016) 31–40, https://doi.org/10.1016/j.molcata.2016.06.004.

[35] A. Solmaz, S. Balci, T. Dogu, Synthesis and characterization of V, Mo and Nb incorporated micro–mesoporous MCM-41 materials, Mater. Chem. Phys. 125 (2011) 148–155, https://doi.org/10.1016/j.matchemphys.2010.08.086.

[36] C. Mahendiran, T. Maiyalagan, P. Vijayan, C. Suresh, K. Shanthi, V-Mn-MCM-41 catalyst for the vapor phase oxidation of o-xylene, React. Kinet. Mech. Catal. 105 (2012) 469–481, https://doi.org/10.1007/s11144-011-0383-3.

[37] Y. Chen, H. Qin, X.B. Shi, Y. Kong, Effects of diameters on the catalytic activity of spherical V-MCM-41 in the selective oxidation of styrene, Adv. Mater. Res. 549 (2012) 137–140, https://dx.doi.org/10.4028/www.scientific.net/AMR.549.137.

[38] K. Wu, B. Li, C. Han, J. Liu, Synthesis, characterization of MCM-41 with high vanadium content in the framework and its catalytic performance on selective oxidation of cyclohexane, Appl. Catal. Gen. 479 (2014) 70–75, https://doi.org/10.1016/j.apcata.2014.04.004.

[39] L.F. Chen, L.E. Noreña, J. Navarrete, J.A. Wang, Improvement of surface acidity and structural regularity of Zr-modified mesoporous MCM-41, Mater. Chem. Phys. 97 (2006) 236–242, https://doi.org/10.1016/j.matchemphys.2005.08.043.

[40] N. Venkatathri, R. Srivastava, Synthesis, characterization and catalytic properties of hexagonal mesoporous vanadium aluminophosphate molecular sieves, Catal. Commun. 6 (2005) 177–183, https://doi.org/10.1016/j.catcom.2004.12.005.

[41] R.R. Langeslay, D.M. Kaphan, C.L. Marshall, P.C. Stair, A.P. Sattelberger, M. Delferro, Catalytic applications of vanadium: a mechanistic perspective, Chem. Rev. 119 (2019) 2128–2191, https://doi.org/10.1021/acs.chemrev.8b00245.

[42] K.M. Reddy, I. Moudrakovski, A. Sayari, Synthesis of mesoporous vanadium silicate molecular sieves, J. Chem. Soc. Chem. Commun. (1994) 1059, https://doi.org/10.1039/c39940001059.

[43] R. Radhakrishnan, C. Reed, S.T. Oyama, M. Seman, J.N. Kondo, K. Domen, Y. Ohminami, K. Asakura, Variability in the structure of supported MoO 3 catalysts: studies using Raman and X-ray absorption spectroscopy with ab initio calculations, J. Phys. Chem. B 105 (2001) 8519–8530, https://doi.org/10.1021/jp0117361.

[44] F.J. Méndez, E. Bastardo-González, P. Betancourt, L. Paiva, J.L. Brito, NiMo/MCM-41 catalysts for the hydrotreatment of polychlorinated biphenyls, Catal. Lett. 143 (2013) 93–100, https://doi.org/10.1007/s10562-012-0933-y.

[45] A. Bielański, M. Najbar, V2O5-MoO3 catalysts for benzene oxidation, Appl. Catal. Gen. 157 (1997) 223–261, https://doi.org/10.1016/S0926-860X(97)00018-5.

[46] N.R. Shiju, V.V. Guliants, Recent developments in catalysis using nanostructured materials, Appl. Catal. Gen. 356 (2009) 1–17, https://doi.org/10.1016/j.apcata.2008.11.034.

[47] M. Selvaraj, T.G. Lee, A novel route to produce phthalic anhydride by oxidation of o-xylene with air over mesoporous V-Mo-MCM-41 molecular sieves, Microporous Mesoporous Mater. 85 (2005) 39–51, https://doi.org/10.1016/j.micromeso.2005.05.046.

[48] A. Teimouri, M. Mahmoudsalehi, H. Salavati, Catalytic oxidative desulfurization of dibenzothiophene utilizing molybdenum and vanadium oxides supported on MCM-41, Int. J. Hydrogen Energy 43 (2018) 14816–14833, https://doi.org/10.1016/j.ijhydene.2018.05.102.

[49] B.R. Cuenya, Synthesis and catalytic properties of metal nanoparticles: size, shape, support, composition, and oxidation state effects, Thin Solid Films 518 (2010) 3127–3150, https://doi.org/10.1016/j.tsf.2010.01.018.

[50] J.R. Croy, S. Mostafa, J. Liu, Y. Sohn, B. Roldan Cuenya, Size dependent study of MeOH decomposition over size-selected Pt nanoparticles synthesized via micelle encapsulation, Catal. Lett. 118 (2007) 1–7, https://doi.org/10.1007/s10562-007-9162-1.

[51] P. Prinsen, R. Luque, (Chapter 1): Introduction to Nanocatalysts. https://doi.org/10.1039/9781788016292-00001, 2019.

[52] S. Bhattacharyya, G. Lelong, M.L. Saboungi, Recent progress in the synthesis and selected applications of MCM-41: a short review, J. Exp. Nanosci. 1 (2006) 375–395, https://doi.org/10.1080/17458080600812757.

[53] R.R. Castillo, L. De La Torre, F. García-Ochoa, M. Ladero, M. Vallet-Regí, Production of MCM-41 nanoparticles with control of particle size and structural properties: optimizing operational conditions during scale-up, Int. J. Mol. Sci. 21 (2020) 1–18, https://doi.org/10.3390/ijms21217899.

[54] S. Olveira, S.P. Forster, S. Seeger, Nanocatalysis: academic discipline and industrial realities, J. Nanotechnol. 2014 (2014) 1–19, https://doi.org/10.1155/2014/324089.

[55] S.O. Lee, T. Tran, B.H. Jung, S.J. Kim, M.J. Kim, Dissolution of iron oxide using oxalic acid, Hydrometallurgy 87 (2007) 91–99, https://doi.org/10.1016/j.hydromet.2007.02.005.

[56] D. Panias, M. Taxiarchou, I. Paspaliaris, A. Kontopoulos, Mechanisms of dissolution of iron oxides in aqueous oxalic acid solutions, Hydrometallurgy 42 (1996) 257–265, https://doi.org/10.1016/0304-386X(95)00104-O.

[57] G. de O. Mendes, T. Dyer, L. Csetenyi, G.M. Gadd, Rock phosphate solubilization by abiotic and fungal-produced oxalic acid: reaction parameters and bioleaching potential, Microb. Biotechnol. 15 (2022) 1189–1202, https://doi.org/10.1111/1751-7915.13792.

[58] G. de O. Mendes, H.M. Murta, R.V. Valadares, W.B. da Silveira, I.R. da Silva, M.D. Costa, Oxalic acid is more efficient than sulfuric acid for rock phosphate solubilization, Miner. Eng. 155 (2020) 106458, https://doi.org/10.1016/j.mineng.2020.106458.

[59] A. Pathak, M. Vinoba, R. Kothari, Emerging role of organic acids in leaching of valuable metals from refinery-spent hydroprocessing catalysts, and potential techno-economic challenges: a review, Crit. Rev. Environ. Sci. Technol. 51 (2021) 1–43, https://doi.org/10.1080/10643389.2019.1709399.

[60] M. Gürü, A.Y. Bilgesü, V. Pamuk, Production of oxalic acid from sugar beet molasses by formed nitrogen oxides, Bioresour. Technol. 77 (2001) 81–86, https://doi.org/10.1016/S0960-8524(00)00122-X.

[61] G.J.G. Ruijter, P.J.I. van de Vondervoort, J. Visser, Oxalic acid production by Aspergillus Niger: an oxalate-non-producing mutant produces citric acid at pH 5 and in the presence of manganese, Microbiology 145 (1999) 2569–2576, https://doi.org/10.1099/00221287-145-9-2569.

[62] O. Adesina, K. Oluwabunmi, E. Betiku, L. Fatuntele, O. Ayodele, C. Adesanwo, Optimzation of process variables for the production of oxalic acid from sweet potato starch hydrozylate 18:16â, Chem. Process Eng. Res. 18 (2014) 16–25.

[63] A.M. Aslam, R.D. Sproull, M.L. Laver, C.J. Biermann, The utilization of douglas-fir bark for the production of oxalic acid and high density carbon pellets, Appl. Biochem. Biotechnol. 20–21 (1989) 135–148, https://doi.org/10.1007/BF02936478.

[64] S.D. Deshpande, S.N. Vyas, Oxidation of sugar to oxalic acid and absorption of oxides of nitrogen to sodium nitrite, Ind. Eng. Chem. Prod. Res. Dev. 18 (1979) 69–71, https://doi.org/10.1021/i360069a015.

[65] Y. Gucbilmez, T. Dogu, S. Balci, Vanadium incorporated high surface area MCM-41 catalysts, Catal. Today 100 (2005) 473–477, https://doi.org/10.1016/j.cattod.2004.10.032.

[66] Q. Zhang, Y. Wang, Y. Ohishi, T. Shishido, K. Takehira, Vanadium-containing MCM-41 for partial oxidation of lower alkanes, J. Catal. 202 (2001) 308–318, https://doi.org/10.1006/jcat.2001.3276.

[67] J.C. Vartuli, K.D. Schmitt, C.T. Kresge, W.J. Roth, M.E. Leonowicz, S.B. McCullen, S.D. Hellring, J.S. Beck, J.L. Schlenker, Effect of surfactant/silica molar ratios on the formation of mesoporous molecular sieves: inorganic mimicry of surfactant liquid-crystal phases and mechanistic implications, Chem. Mater. 6 (1994) 2317–2326, https://doi.org/10.1021/cm00048a018.

[68] S.K. Amit, M.M. Uddin, R. Rahman, S.M.R. Islam, M.S. Khan, A review on mechanisms and commercial aspects of food preservation and processing, Agric. Food Secur. 6 (2017) 51, https://doi.org/10.1186/s40066-017-0130-8.

[69] C.N. Njoku, S.K. Otisi, Application of central composite design with design expert v13 in process optimization, in: Response Surf. Methodol, Res. Adv. Appl., IntechOpen, 2023, p. 13, https://doi.org/10.5772/intechopen.109704.

[70] A. Teimouri, M. Mahmoudsalehi, H. Salavati, Catalytic oxidative desulfurization of dibenzothiophene utilizing molybdenum and vanadium oxides supported on MCM-41, Int. J. Hydrogen Energy 43 (2018) 14816–14833, https://doi.org/10.1016/j.ijhydene.2018.05.102.

[71] L.A. Cortes, J.R. Simpson, P.A. Parker, Response surface split-plot designs: a literature review, Qual. Reliab. Eng. Int. 34 (2018) 1374–1389, https://doi.org/10.1002/qre.2350.

[72] Q. Huo, D.I. Margolese, G.D. Stucky, Surfactant control of phases in the synthesis of mesoporous silica-based materials, Chem. Mater. 8 (1996) 1147–1160, https://doi.org/10.1021/cm960137h.

[73] M.D. Donohue, G.L. Aranovich, Classification of Gibbs adsorption isotherms, Adv. Colloid Interface Sci. 76–77 (1998) 137–152, https://doi.org/10.1016/S0001-8686(98)00044-X.

[74] M. Thommes, K. Kaneko, A.V. Neimark, J.P. Olivier, F. Rodriguez-Reinoso, J. Rouquerol, K.S.W. Sing, Physisorption of gases, with special reference to the evaluation of surface area and pore size distribution (IUPAC Technical Report), Pure Appl. Chem. 87 (2015) 1051–1069, https://doi.org/10.1515/pac-2014-1117.

[75] A. Trouvé, I. Batonneau-Gener, S. Valange, M. Bonne, S. Mignard, Tuning the hydrophobicity of mesoporous silica materials for the adsorption of organic pollutant in aqueous solution, J. Hazard Mater. 201–202 (2012) 107–114, https://doi.org/10.1016/j.jhazmat.2011.11.043.

[76] A. Corma, From microporous to mesoporous molecular sieve materials and their use in catalysis, Chem. Rev. 97 (1997) 2373–2420, https://doi.org/10.1021/cr960406n.

[77] B. Nassima, B. Abdallah, D. Abdelkader, Synthesis and Modification of a Mesoporous Material Type MCM-41 by an Amine for the Adsorption of Organic Pollutants: Anionic and Cationic Dyes, BioRxiv, 2017 118182, https://doi.org/10.1101/118182.

[78] D.M. Oliveira, A.S. Andrada, Synthesis of ordered mesoporous silica MCM-41 with controlled morphology for potential application in controlled drug delivery systems, Cerâmica 65 (2019) 170–179, https://doi.org/10.1590/0366-69132019653742509.

[79] J. Xu, W. Chu, S. Luo, Synthesis and characterization of mesoporous V-MCM-41 molecular sieves with good hydrothermal and thermal stability, J. Mol. Catal. Chem. 256 (2006) 48–56, https://doi.org/10.1016/j.molcata.2006.03.078.

[80] D.S. Lee, T.K. Liu, Characterization of V-MCM-41 mesoporous materials, J. Sol. Gel Sci. Technol. 24 (1) (2002 May) 69–80, https://doi.org/10.1023/A:1015165600804 (n.d.).

[81] R. Kumar Rana, B. Viswanathan, Mo incorporation in MCM-41 type zeolite, Catal. Lett. 52 (1998) 25–29, https://doi.org/10.1023/A:1019019403375.

[82] X. Wang, G. Zhou, Z. Chen, W. Jiang, H. Zhou, In-situ synthesis and characterization of V-MCM-41 for oxidative dehydrogenation of n-butane, Microporous Mesoporous Mater. 223 (2016) 261–267, https://doi.org/10.1016/j.micromeso.2015.06.029.

[83] Ü. Gedikli, Z. Misirlioğlu, A. Bozkurt, M. Canel, Synthesis and characterization of mcm-41 and metal-supported mcm-41 materials using different methods, Commun. Fac. Sci. Univ. Ankara Ser. B Chem. Chem. Eng. 62 (2020) 23–39.

[84] F.S. Bastos, O.A. Lima, C. Raymundo Filho, L.D. Fernandes, Mesoporous molecular sieve MCM-41 synthesis from fluoride media, Braz. J. Chem. Eng. 28 (2011) 649–658, https://doi.org/10.1590/S0104-66322011000400010.

[85] V.M. Vaschetti, G.A. Eimer, A.L. Cánepa, S.G. Casuscelli, Catalytic performance of V-MCM-41 nanocomposites in liquid phase limonene oxidation: vanadium leaching mitigation, Microporous Mesoporous Mater. 311 (2021) 110678, https://doi.org/10.1016/j.micromeso.2020.110678.

[86] K. Wu, B. Li, C. Han, J. Liu, Synthesis, characterization of MCM-41 with high vanadium content in the framework and its catalytic performance on selective oxidation of cyclohexane, Appl. Catal. Gen. 479 (2014) 70–75, https://doi.org/10.1016/j.apcata.2014.04.004.

[87] T.S. Reddy, M.C.S. Kumar, Effect of substrate temperature on the physical properties of co-evaporated Sn2S3 thin films, Ceram. Int. 42 (2016) 12262–12269, https://doi.org/10.1016/j.ceramint.2016.04.172.

[88] I. Kariper, Optical and structural properties of CdSe thin film produced by chemical bath deposition, J. Non-Oxide Glas 1 (2016), 1–9.

[89] P.E. Boahene, K. Soni, A.K. Dalai, J. Adjaye, Hydrotreating of coker light gas oil on Ti-modified HMS supports using Ni/HPMo catalysts, Appl. Catal. B Environ. 101 (2011) 294–305, https://doi.org/10.1016/j.apcatb.2010.09.030.

[90] S.A. Jabasingh, G. Pavithra, Response surface approach for the biosorption of Cr6+ ions by Mucor racemosus, Clean - soil, Air, Water 38 (2010) 492–499, https://doi.org/10.1002/clen.200900270.

[91] Z.N. Garba, I. Bello, A. Galadima, A.Y. Lawal, Optimization of adsorption conditions using central composite design for the removal of copper (II) and lead (II) by defatted papaya seed, Karbala Int. J. Mod. Sci. 2 (2016) 20–28, https://doi.org/10.1016/j.kijoms.2015.12.002.